

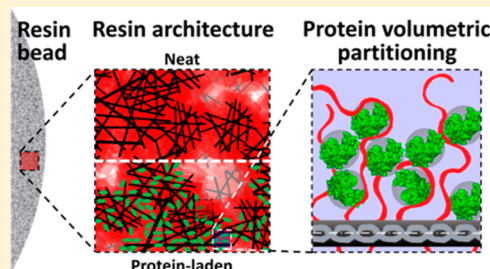
# Effects of Resin Architecture and Protein Size on Nanoscale Protein Distribution in Ion-Exchange Media

Stijn H. S. Koshari, Norman J. Wagner,<sup>1</sup> and Abraham M. Lenhoff<sup>1\*</sup>

Center for Molecular and Engineering Thermodynamics, Department of Chemical and Biomolecular Engineering, University of Delaware, 150 Academy Street, Newark, Delaware 19716, United States

## Supporting Information

**ABSTRACT:** Knowledge of the nanoscale distribution of proteins in chromatographic resins is critical to our mechanistic understanding of separations performance. However, the nano- to mesoscale architecture of these materials is challenging to characterize using conventional techniques. Small-angle neutron scattering was used to probe (1) the nano- to mesoscale structure of chromatographic media and (2) protein sorption in these media in situ with protein-scale resolution. In particular, we characterize the effect of the architecture of cellulose-based and traditional and dextran-modified agarose-based ion-exchange resins on the nanoscale distribution of a relatively small protein (lysozyme) and two larger proteins (lactoferrin and a monoclonal antibody) at different protein loadings. Traditional agarose-based resins (SP Sepharose FF) can be envisioned as comprising long, thin strands of helical resin material around which the proteins adsorb, while higher static capacities are achieved in dextran-modified resins (SP Sepharose XL and Capto S) due to protein partitioning into the increased effective binding volume provided by the dextran. While protein size is shown not to affect the underlying sorption behavior in agarose-based resins such as SP Sepharose FF and XL, it plays an important role in the cellulose-based S HyperCel and the more highly cross-linked agarose-based Capto S, where size-exclusion effects prevent larger proteins from binding to the base matrix resin strands. Based on the data, we propose that entropic partitioning effects such as depletion forces may drive the observed protein crowding. In general, these observations elucidate the structure and point to the mechanism of protein partitioning in different classes of chromatographic materials, providing guidance for optimizing their performance.



## INTRODUCTION

The distribution of sorbed proteins within chromatographic resins is thought to affect separation performance by affecting uptake rate and capacity. Current design strategies to improve chromatographic resins include influencing the protein distribution through manipulation of the resin architecture, including the use of highly porous resin matrices and polymer-modification.<sup>1–4</sup> As opposed to traditional resins, for which proteins adsorb as monolayers directly on the surface of the base matrix, polymer-modified materials contain functionalized polymers that allow volumetric protein partitioning into the polymer-occupied space.<sup>5,6</sup> Although such advances have led to resins with improved performance, especially in terms of binding capacities, mechanistic understanding of the underlying structural interactions between proteins and the architecture of these resins is currently incomplete. For example, polymer extenders can decrease the effective mesh size and lead to size-exclusion effects that are not present in traditional materials. Consequently, detailed measurements of resin architecture and sorbed protein distribution can improve our understanding of resin performance and aid in the design of superior materials.

Nanoscale characterization of protein adsorption within the resin architecture is challenging with conventional methods. While imaging techniques such as optical, fluorescence, or electron microscopy can visualize the micro- and macro-

structure of the resins, they lack the resolution required to study the structure on the length scale of the protein.<sup>7–11</sup> In addition, microscopy techniques often require drying, chemical fixation, or fluorescence labeling of the protein, which raises concerns about whether the observed structural information is an accurate representation of the structure under normal operating conditions.<sup>10–12</sup> Conversely, characterization techniques such as gas adsorption or inverse size-exclusion chromatography (ISEC) can measure general structural parameters such as the total surface area and the pore size distribution of the resins, but they do not allow detailed visualization of the resin architecture and are challenging to use after protein sorption.<sup>6,10,13–16</sup> Hence, a true nanoscale characterization of protein distribution in chromatographic resins requires a technique with protein-scale resolution that allows in situ characterization without modification of the protein.

In prior research, we developed the method of small-angle neutron scattering (SANS) to characterize resin architecture and protein distribution within chromatographic resins.<sup>17</sup> SANS is particularly well-suited to study these systems as it is

Received: September 18, 2017

Revised: November 22, 2017

capable of capturing structural features from the nanometer to the micrometer length scale, can probe relatively large sample volumes, can penetrate opaque materials to determine internal structure, and is minimally disruptive.<sup>18–22</sup> The adsorption of lysozyme on a cellulose-based chromatographic material, S HyperCel, was studied to validate the method and create a framework to support further investigation of chromatographic materials.<sup>17,23</sup> Importantly, we demonstrated that SANS is capable of quantifying the nano- and microscale fractal architecture of S HyperCel and the nanoscale distribution of lysozyme in this material, which manifests as a densification of the sorbent's fractal network. Furthermore, quantitative analysis of SANS measurements determined the amount of sorbed protein under relevant physicochemical conditions. These findings support the view that adsorption in this resin shows similarities to volumetric partitioning in polymer-modified resins because of the high cross-link density and consequent fractal nature of the cellulose base matrix, explaining the material's high static and dynamic binding capacities for small proteins.<sup>10,11</sup>

In the present work, we study the nano- to mesoscale architectures of three fundamentally different resins: a traditional agarose-based resin (SP Sepharose Fast Flow) and two dextran-modified agarose-based resins (SP Sepharose XL and Capto S), in addition to the previously studied S HyperCel. The four resins are referred to in this report simply as FF, XL, Capto, and HyperCel, respectively. These materials have been extensively studied before, in terms of both performance as well as structural characterization using conventional techniques such as ISEC and microscopy techniques.<sup>6–11,13,24</sup> As a hypothesis, we propose that the size of proteins will affect their sorbed distribution at the nanoscale in these different chromatographic media. To test this, we use SANS to quantify the nanostructural changes in these resins after adsorption of lysozyme, lactoferrin, and a monoclonal antibody (mAb) under varying loadings.

## EXPERIMENTAL SECTION

**Materials. Buffers.** Monobasic sodium phosphate ( $\text{NaH}_2\text{PO}_4$ ) and sodium chloride ( $\text{NaCl}$ ) were purchased from Fisher Scientific (Waltham, MA), deuterium oxide ( $\text{D}_2\text{O}$ ) at 99.8 atom % D was purchased from Cambridge Isotope Laboratories, Inc. (Tewksbury, MA), and acetic acid was purchased from Sigma-Aldrich (St. Louis, MO). They were used to prepare 10 mM sodium phosphate buffer solutions at pH 7 and 10 mM acetic acid buffer solutions at pH 5 in both deionized (DI) water ( $\text{H}_2\text{O}$ ) and  $\text{D}_2\text{O}$ . The total ionic strength (TIS) in the solutions was adjusted using  $\text{NaCl}$  to 20, 50, 100, and 200 mM TIS.

**Protein Solutions.** Hen egg white lysozyme (molecular weight [MW] 14.3 kDa) was purchased from Sigma-Aldrich, recombinant human lactoferrin (MW 78 kDa) was purchased from Lee BioSolutions (Maryland Heights, MO), and an IgG2 monoclonal antibody (mAb, MW 144 kDa, pI 7.9) was provided by Amgen, Inc. (Thousand Oaks, CA). The lysozyme and lactoferrin were prepared by dissolving the lyophilized proteins in each of the four TIS-controlled, sodium phosphate pH 7 buffers in  $\text{H}_2\text{O}$ , while the mAb was provided in a concentrated solution and diluted with each of the four TIS-controlled, acetic acid pH 5 buffers in  $\text{H}_2\text{O}$  before buffer exchange. Subsequently, protein solutions were buffer-exchanged three times with the appropriate pH 7 (lysozyme and lactoferrin) or pH 5 (mAb)  $\text{H}_2\text{O}$ -based buffer, using either 3 or 50 kDa Amicon Ultra-15 centrifugal filters from Millipore (Billerica, MA). Concentrated protein solutions were filtered at  $0.22 \mu\text{m}$  and concentrations were determined using UV spectrophotometry (Thermo Scientific NanoDrop 2000, Waltham, MA).

**Chromatographic Media.** S HyperCel (lot AU31072012-4) was provided by Pall Corporation (Northborough, MA). SP Sepharose Fast Flow (lot 10224983), SP Sepharose XL (lot 311563), and Capto S (lot 10061582) were obtained from GE Healthcare (Piscataway, NJ). All four resins are functionalized for cation exchange (CEX) with a sulfonate ligand; other key properties of these resins have been reported before.<sup>7–11</sup> FF and XL have the same agarose base matrix, but 40 kDa dextran is grafted onto XL, which can result in the attachment of each dextran molecule at more than one point. Both resins are functionalized with the same sulfonate group on a six-carbon spacer arm. Conversely, Capto uses the same 40 kDa dextran extenders as XL, but it has a more highly cross-linked agarose base matrix and is functionalized with a sulfonate group on a two-carbon spacer arm. HyperCel is synthesized from a highly cross-linked cellulosic base matrix and functionalized with a sulfonate ligand without a spacer arm. The relatively narrow pore structure of HyperCel has been compared to that of the dextran-modified resins.<sup>11</sup> Consequently, these resins are suitable for making direct structural comparisons. The average particle diameter is reported to be  $90 \mu\text{m}$  for the agarose-based resins<sup>7</sup> and  $75\text{--}80 \mu\text{m}$  for HyperCel.<sup>10</sup>

The chromatographic particles were washed three times by suspending in DI  $\text{H}_2\text{O}$  and then centrifuging and decanting. This was followed by solvent exchange with  $\text{D}_2\text{O}$  by repeating this procedure twice by suspending in  $\text{D}_2\text{O}$  and letting the solution equilibrate for a 12 h interval.

**Sample Preparation.** Each of the four resins was investigated “neat” without adsorbed protein as well as after adsorption of the three proteins, leading to 16 resin–protein combinations. Each of these combinations was investigated at four TIS conditions, 20, 50, 100, and 200 mM TIS, to influence the protein loading, leading to a total of 64 resin–protein samples, which include neat samples with no protein.

To measure the structure of the neat chromatographic media, the 16 samples were prepared by equilibrating 0.5 mL of hydrated particle volume (hvp) of chromatographic particles with 9.5 mL of the appropriate TIS-controlled sodium phosphate buffer in  $\text{D}_2\text{O}$ . After equilibration by gentle end-over-end rotation over a 48 h period, the settled chromatographic particle slurry was separated from the supernatant to use in the neutron scattering experiment.

To measure protein uptake, each of the 48 protein-laden samples was prepared with (1) 0.5 mL of hydrated particle volume (hvp) of chromatographic media equilibrated with pure  $\text{D}_2\text{O}$ , (2) a certain volume of concentrated protein solution in the appropriate TIS-controlled  $\text{H}_2\text{O}$  buffer, determined by the desired final protein concentration, and (3) the appropriate pH 5 or pH 7 TIS-controlled  $\text{D}_2\text{O}$  buffer solution to bring the total sample volume to 10 mL. Samples were equilibrated by gentle rotation over a 48 h period, after which protein concentrations in the supernatant solutions were measured using UV spectrophotometry (Thermo Scientific NanoDrop 2000). The settled particle suspension, consisting of approximately 10 vol % protein, 20 vol % particles, and 70 vol % water, depending on the sample, was separated from the supernatant to use in the neutron scattering experiment.

**Sample Compositions.** For each resin–protein combination, the added amount of concentrated protein solution at each of the four TISs was specifically selected such that sorbed protein concentrations would vary within the resin–protein combination, while keeping the supernatant protein concentration after adsorption around 1 mg/mL. The added amounts of protein were based on previous adsorption isotherm data for these resin–protein combinations.<sup>7,11</sup> The supernatant protein concentration of 1 mg/mL was chosen such that the protein loading would lie well within the plateau region of the adsorption isotherms and the static binding capacity of the resins for the specific protein and TIS conditions was approached.

The adsorbed amount  $q$  (mg/mL hvp) was determined by mass balance

$$q = \frac{V}{V_m}(C_0 - C) \quad (1)$$

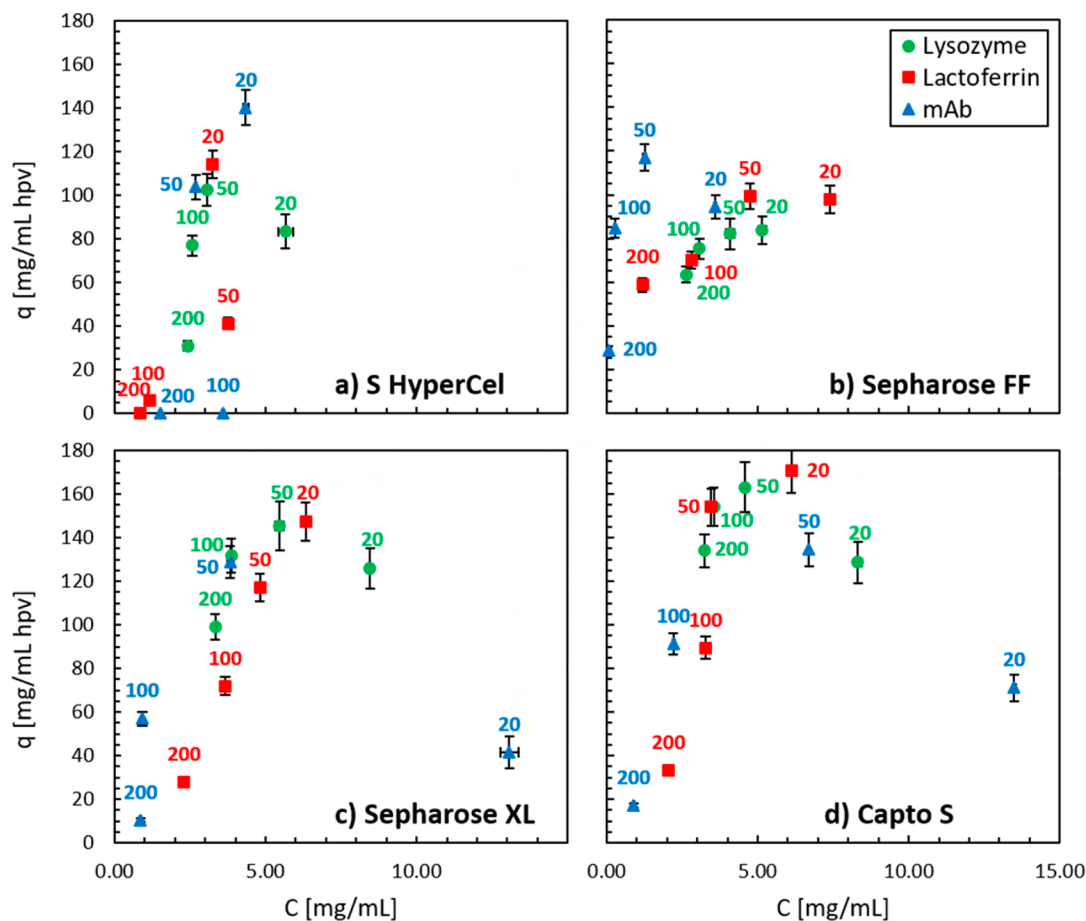


**Figure 1.** Adsorbed protein concentrations in the chromatographic media as a function of supernatant concentration. Labels indicate the approximate total ionic strength (TIS) of each sample.

where  $V$  (mL) is the total solution volume,  $V_m$  (mL hpv) is the hydrated particle volume (hpv),  $C_0$  (mg/mL) is the initial protein concentration, and  $C$  (mg/mL) is the final protein concentration in the supernatant. Figure 1 shows the protein loadings obtained for each resin–protein combination. Each point in this figure is a single point of the protein adsorption isotherm, typically lying in the plateau region of the isotherm. The observed trends in protein loading generally correspond well to protein adsorption isotherm data measured previously, with decreased protein loading at higher TISs. However, for a few samples at 20 mM, the protein loading is significantly lower than expected from previous isotherm data, e.g., mAb in agarose-based resins. Additionally, previous data show higher adsorbed amounts than measured here,<sup>7,11</sup> which is also reflected in the fact that the supernatant protein concentrations are generally slightly higher than the intended 1 mg/mL. The lower adsorption might be due to several factors, including slow protein uptake at very low TIS<sup>25</sup> and D<sub>2</sub>O being a major component of the solvent instead of just H<sub>2</sub>O. However, these observations do not compromise further structural analysis from the SANS spectra.

Small amounts of H<sub>2</sub>O are introduced into the samples via the concentrated protein solutions, leading to varying D<sub>2</sub>O/H<sub>2</sub>O fractions in the solvent of the samples. As the amount of H<sub>2</sub>O in the sample has an important effect on the background scattering, scattering length density, and overall scattering intensity, these variations in D<sub>2</sub>O:H<sub>2</sub>O fraction were taken into consideration during analysis of the scattering spectra.

**Methods. Small-Angle Neutron Scattering.** The theoretical background on small-angle neutron scattering (SANS) has been discussed extensively in prior work.<sup>17</sup> Concisely, SANS can probe structural heterogeneities within the sample by measuring the intensity

$I(Q)$  of deflected neutrons at a certain angle from the incident beam,  $\theta$ , which for simple systems can be described as<sup>20–22</sup>

$$I(Q) \propto (\Delta\rho)^2 P(Q) S(Q) + B \quad (2)$$

in which

$$Q = \frac{4\pi}{\lambda} \sin \frac{\theta}{2} \quad (3)$$

is the magnitude of the momentum transfer vector,  $\lambda$  is the wavelength of the neutrons, and  $\rho$  is the scattering length density (SLD), which is material-dependent and determines the scattering contrast in the sample. As  $Q$  is related to the length scale being probed,  $L$ , by Bragg's law<sup>20</sup>

$$L = \frac{2\pi}{Q} \quad (4)$$

features observed in SANS spectra contain structural information of the sample on these real-space length scales. This structural information is represented in eq 2 by the form factor  $P(Q)$ , which represents the contribution of the shape of the particles or building blocks in the system to the scattering intensity, and the effective structure factor  $S(Q)$ , which represents the contribution of the interactions among these components. The background scattering  $B$  is typically observed in the high- $Q$  region of the spectrum and depends on sample composition but provides no structural information.

The experiments were carried out on the 30 m NG7 SANS instrument at the NIST Center for Neutron Research (NCNR), National Institute of Standards and Technology (NIST), Gaithersburg, MD.<sup>26</sup> The diffractometer settings for the tests were:

- high  $Q$ : 1 m sample-to-detector distance (SDD) with 6 Å neutrons for a 360 s count time,
- intermediate  $Q$ : 4 m SDD with 6 Å neutrons for a 600 s count time, and
- low  $Q$ : 13 m SDD with lenses with 8 Å neutrons for a 900 s count time.

When spliced together, these regions result in a scattering range  $0.001 \text{ \AA}^{-1} < Q < 0.4 \text{ \AA}^{-1}$ , corresponding to length scales ranging from  $\sim 6000$  to  $\sim 10 \text{ \AA}$ . Demountable quartz window sample cells with a path length (thickness) of 1 mm were used for all samples and a wavelength spread of 0.15 was used for all experiments. Standard data reduction procedures were followed using the program IGOR Pro to obtain corrected and radially averaged SANS scattering spectra.<sup>27</sup> Instrument corrections were applied to the models for comparison with data and the effects of instrumental smearing on the parameter values were determined to be negligible during model fitting using IGOR Pro.

**Structural Models.** The SANS spectra were modeled by standard expressions to obtain quantitative structural information, namely, (1) the generalized Guinier–Porod model<sup>28</sup> for the cellulose-based resin and (2) the polydisperse cylinder model<sup>29</sup> for the agarose-based resins. These models were used to fit the scattering spectra of the resins regardless of the presence of adsorbed protein as they accurately fit the scattering data both before and after protein adsorption.

The generalized Guinier–Porod model is an empirical model that successfully describes the nano- to mesoscale structure of Hyper-Cel.<sup>17,23</sup> The model describes a material with a fractal nature and is given by<sup>28</sup>

$$I(Q) = \frac{G}{Q^s} \exp\left[\frac{-Q^2 R_g^2}{3-s}\right] + B \quad \text{for } Q \leq Q_1 \quad \text{and}$$

$$I(Q) = \frac{D}{Q^m} + B \quad \text{for } Q > Q_1 \quad (5)$$

in which

$$Q_1 = \frac{1}{R_g} \sqrt{\frac{(m-s)(3-s)}{2}} \quad \text{and}$$

$$D = G \exp\left[\frac{-Q_1^2 R_g^2}{3-s}\right] Q_1^{m-s} \quad (6)$$

based on continuity constraints. In these expressions,  $B$  is the background scattering,  $G$  is a scaling coefficient,  $R_g$  is the radius of gyration, and  $m$  and  $s$  are the Porod exponent and the dimension variable, which are related to the fractal dimensions of the microstructure on short and long real-space length scales, respectively. The radius of gyration can be obtained from the  $Q$ -value at the inflection point  $Q_1$  between the two fractal regions. Hence, this radius of gyration is a characteristic average length scale within the particle structure, with length scales below the  $R_g$  characterized by a fractal dimension related to the Porod exponent and length scales above the  $R_g$  characterized by a fractal dimension related to the dimension variable.

The SANS spectra from the agarose-based resins were fit using a polydisperse cylinder model, which represents a collection of noninteracting cylinders with a mean radius  $R$  and length  $L$ . Polydispersity of the cylinder radius is modeled using a normalized log-normal distribution  $n(r)$ . For this model, the scattering intensity as a function of  $Q$  is calculated as<sup>29</sup>

$$I(Q) = \frac{\phi}{V} (\rho_{\text{cyl}} - \rho_{\text{sol}})^2 \iint n(r) F^2(Q, r, \alpha) \sin \alpha \, dr + B \quad (7)$$

in which

$$V = \pi R^2 L$$

$$n(r) = \frac{\exp\left[-\frac{1}{2} \left(\frac{\ln(r/R)}{\sigma}\right)^2\right]}{\sqrt{2\pi} \sigma R}, \quad \text{and}$$

$$F(Q, r, \alpha) = 2Vj_0\left(\frac{QL \cos \alpha}{2}\right) \frac{J_1(Qr \sin \alpha)}{Qr \sin \alpha} \quad (8)$$

The seven fitting parameters are (1) the volume fraction  $\phi$ , (2) the mean radius  $R$ , (3) the length  $L$ , (4) the radial polydispersity  $\sigma$ , which is equal to the standard deviation of the log-normal distribution, (5) the SLD of the cylinder  $\rho_{\text{cyl}}$ , (6) the SLD of the solvent  $\rho_{\text{sol}}$ , and (7) the background  $B$ . The polydisperse cylinder model is a two-phase model, one phase consisting of the cylinders and one phase consisting of the solvent. In such models, the SLD values of the two phases affect only the overall scaling of the scattering intensity, not the shape of the scattering spectrum and consequently not the other structural parameters of the model except the volume fraction, which also scales directly with the scattering spectrum.

**Protein Form Factors.** Equation 2 can be applied directly to protein systems within a framework in which the form factor  $P(Q)$  is the protein monomers' characteristic scattering pattern due to their shape, while the effective structure factor  $S(Q)$  is due to local interactions in solution, clustering, and aggregation. Both of these can have an effect on the total scattering spectrum from protein solutions. However, in dilute protein solutions, the structure factor contribution becomes negligible and the protein form factor can be directly obtained from SANS measurements. The form factors of the three proteins were measured experimentally by SANS after dilution of the concentrated protein solutions to approximately 5 mg/mL in the pH 7 (lysozyme and lactoferrin) or pH 5 (mAb) buffer in  $D_2O$  at 20 mM TIS, a concentration low enough to minimize contributions from the protein structure factor. The experimental form factors of the three proteins are shown in Figure 2.

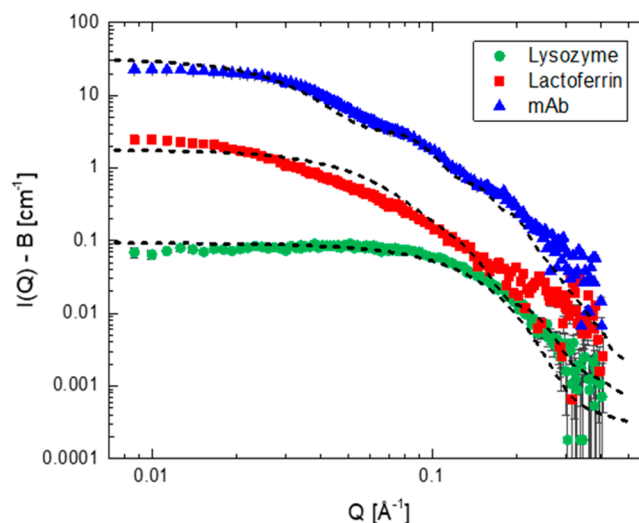


**Figure 2.** Scattering spectra of protein solutions at low concentrations (approximately 5 mg/mL), showing the characteristic scattering spectrum of protein monomers, i.e., the protein form factor. CRYSON scattering predictions from protein PDB files are shown by the dashed lines. Successive curves are offset by a factor of 4 for clarity.

The scattering spectrum contribution from the form factor is calculated directly from the atomic structure of the protein using the program CRYSON<sup>30</sup> as applied to structural data from the RCSB Protein Data Bank (PDB).<sup>31</sup> These calculations can take effects such as the solvation shell (not applied here) and the solvent composition (100 mol %  $D_2O$ ) into account. The CRYSON output is the form factor of a single protein monomer in units of barn ( $1 \text{ b} = 10^{-28} \text{ m}^2$ ).

The scattering spectrum scales linearly with the protein concentration, so the concentration of the protein can be taken into account by multiplication of the calculated scattering spectrum by the protein concentration. Thus, the protein monomer contribution can be predicted from the protein concentration in the system, or conversely, the protein concentration can be determined from its contribution to the scattering intensity.

CRYSON was used to compare the experimentally measured form factors to the values calculated from the protein atomic structures. The PDB files used to model lysozyme, lactoferrin, and the mAb have the PDB IDs 6LYS,<sup>32</sup> 2BJJ,<sup>33</sup> and 1IGT,<sup>34</sup> respectively. The CRYSON predictions are shown by the dashed lines in Figure 2. They capture the experimentally determined structure factors fairly well, although small deviations can be observed for each protein in specific regions. These deviations can be caused by the flexibility of the protein structure in solution, such as mAb hinge motions, as opposed to the crystalline protein structure obtained from the PDB files. Consequently, such small deviations can be expected and the CRYSON predictions adequately confirm the experimentally determined form factors, which are used to characterize protein adsorption in the chromatographic resins.

**Model Fitting of Neat Resins.** For the neat resins with no adsorbed protein, structural models described the scattering spectra well over the whole  $Q$  range, and the models could consequently be directly fit to the experimental data using IGOR Pro's NCNR Analysis Macros.<sup>27</sup> For the generalized Guinier-Porod model for HyperCel, no parameters were held fixed during the fitting process, generally resulting in five fitting parameters. For the polydisperse cylinder model for agarose-based resins, the cylinder length and the SLD values were held fixed during fitting. The model described the experimental data well for cylinders that were effectively infinitely long. Hence, the cylinder length was fixed at 10 000 Å to simplify the model and reduce the number of fitting parameters to four.

SLD values for the base matrix and the solvent were calculated using the NCNR SLD Calculator,<sup>35,36</sup> for which the molecular densities were calculated from the displaced solvent volumes of the ensemble atomic groups.<sup>37</sup> The SLD of pure D<sub>2</sub>O and of the agarose base matrix in pure D<sub>2</sub>O were calculated to be  $6.33 \times 10^{-6}$  and  $2.22 \times 10^{-6} \text{ \AA}^{-2}$ , respectively. Note that the SLD of polymers such as agarose and proteins can change depending on the D<sub>2</sub>O content of the surrounding environment due to deuterium exchange. For these calculations, it was assumed that the fraction of exchanged hydrogens on the polymer was equal to the fraction of D<sub>2</sub>O in the solvent (100% for the neat resins). Contributions to the solvent SLD from buffer components and to the cylinder SLD from sulfonate ligands and dextran extenders were assumed to be negligible to simplify model calculations. Deviations due to such contributions are effectively all included in the fitted volume fraction and polydispersity.

**Model Fitting of Protein-Laden Resins.** To first order, one might expect that the scattering spectra from protein-laden resins can be modeled by a summation of the scattering spectra from the neat resins and the protein monomer form factor. However, the sorption of the protein to the resin can introduce changes to both the apparent nanostructure of the resin as well as the proteins' contribution to the scattering. Indeed, as the resin and protein have similar scattering length densities, protein distribution into the available space within the resins will be perceived by SANS as an apparent change of the resin nanostructure. Furthermore, resin-protein and protein-protein interactions can lead to changes in the protein scattering contribution. Regardless of these changes, the same structural models with different parameters can be used for the protein-laden resins as the neat resins, with the exception of the high- $Q$  region, where explicit protein contributions are evident. This region was instead fit directly to the expected form factor scattering from the protein monomers. More detailed information on the modeling of protein-laden resins, including specific fitting ranges and fixed fitting parameters, are included in the Supporting Information.

## RESULTS AND DISCUSSION

SANS spectra were measured for four resins (HyperCel, FF, XL, and Capto) and three proteins (lysozyme, lactoferrin, and a mAb), in addition to the neat resin structure with no adsorbed protein, leading to 16 resin-protein configurations. Each configuration was studied at four different total ionic strengths, which affect the total protein loading. This results in a total of 64 scattering spectra, of which only a select few are shown directly here for brevity. However, all scattering spectra and model parameters are included in the Supporting Information.

**Scattering Spectra of Neat Resins.** The reduced scattering spectra of the four resins at 50 mM TIS are shown in Figure 3; symbols represent the experimental data, while the

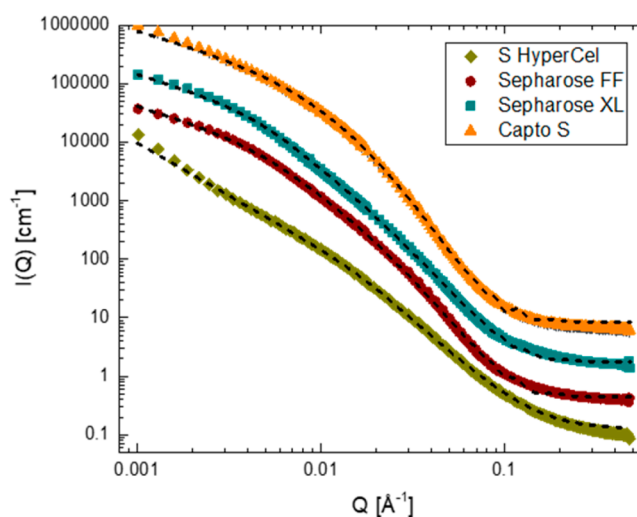


**Figure 3.** Scattering spectra of neat chromatographic media at 50 mM total ionic strength. Model fits are shown in the dashed lines. Successive curves are offset by a factor of 4.

dashed lines show the model fits. HyperCel is modeled by the generalized Guinier-Porod model, while the agarose-based resins are modeled by the polydisperse long-cylinder model. Fitting parameters are provided in Tables 1 and 2. The

**Table 1. Fitting Parameters of the Generalized Guinier-Porod Model and Fitting Values for Neat and Protein-Laden S HyperCel**

	neat <sup>a</sup>	lysozyme <sup>a</sup>	lactoferrin <sup>a</sup>	mAb <sup>a</sup>
scale $G$ [-]	0.040	0.005	0.019	0.012
radius of gyration $R_g$ [Å]	33.5	35.9	33.4	31.2
dimension variable $s$ [-]	1.79	2.17	1.80 <sup>b</sup>	1.80 <sup>b</sup>
Porod exponent $m$ [-]	2.72	2.65	2.70 <sup>b</sup>	2.70 <sup>b</sup>
background $B$ [ $\text{cm}^{-1}$ ]	0.13	0.21	0.21	0.24

<sup>a</sup>Table values include only samples at 50 mM total ionic strength. Fitting values for all samples are included in the Supporting Information. <sup>b</sup>Values were held fixed during fitting.

HyperCel model parameters agree with those found previously.<sup>17</sup> The Porod exponent  $m$  is related to the fractal dimension within individual resin strands, while the dimension variable  $s$  is related to the fractal dimension of the larger resin strand network. The average radius of gyration in the model fits, which can be associated with the radius of gyration of the resin strands, is 34 Å.

**Table 2. Fitting Parameters of the Polydisperse Cylinder Model and Fitting Values for Neat Agarose-Based Resins.**

	SP Sepharose FF <sup>a</sup>	SP Sepharose XL <sup>a</sup>	Capto S <sup>a</sup>
volume fraction $\phi$ [-]	0.034	0.025	0.049
mean cylinder radius $R$ [Å]	13.8	3.2	52.0
radial polydispersity $\sigma$ [-]	0.92	1.26	0.57
cylinder length $L$ [Å] <sup>b</sup>	10 000	10 000	10 000
SLD cylinder $\rho_{\text{cyl}}$ [ $10^{-6} \text{ Å}^{-2}$ ] <sup>b</sup>	2.22	2.22	2.22
SLD solvent $\rho_{\text{solv}}$ [ $10^{-6} \text{ Å}^{-2}$ ] <sup>b</sup>	6.33	6.33	6.33
background $B$ [ $\text{cm}^{-1}$ ]	0.12	0.11	0.15

<sup>a</sup>Table values include only samples at 50 mM total ionic strength. Fitting values for all samples are included in the [Supporting Information](#). <sup>b</sup>Values were held fixed during fitting.

For the agarose-based resins, in FF and XL the mean cylinder radii are 14 and 3 Å and the radial polydispersities  $\sigma$  are 0.9 and 1.3, respectively. In the more densely cross-linked Capto, the mean cylinder radius is 51 Å and the polydispersity is 0.6. The measured volume fractions of the cylinders range from 3 to 5%, which is consistent with the use of 4% agarose in Sepharose FF beads (Sepharose 4). For the neat resins, these parameters are not strongly affected by changing the TIS.

**Nano- to Mesoscale Architecture of Neat Resins.** The cellulose-based HyperCel has an architecture that is fundamentally different from that of the agarose-based resins. HyperCel is well-described by the generalized Guinier-Porod model, which indicates fractal character on two distinct length scales: (1) a dense fractal network of cellulose within the resin fibrils, as indicated by the Porod exponent  $m$ , and (2) a more open fractal network of the resin fibrils themselves on longer length scales, as indicated by the dimension variable  $s$ . These observations correspond to previous SANS measurements on HyperCel and explain why this resin shows performance

comparable to that of polymer-modified materials.<sup>17</sup> However, the generalized Guinier–Porod model is incapable of capturing the architecture of agarose-based resins, which indicates that these materials are inherently not fractal-like. Instead, these materials are better described by the polydisperse cylinder model, in which the cylinder length is very long compared to the cylinder radius. Consequently, the resin strands of which these materials are composed are not intrinsically arranged in a fractal network.

These observations agree well with previously known information on the molecular structure of these materials. While cellulose gels are generally composed of a random polymer network, X-ray diffraction experiments have shown that agarose appears as rigid single or double helices of about 15 Å in diameter in the gel state.<sup>38–41</sup> Comparison with electron microscopy imaging, which shows filaments on the order of 20–300 Å, has led to the hypothesis that these filaments are composed of up to hundreds of agarose helices in a side-by-side assembly.<sup>7,9,10,38,42</sup>

SANS provides an independent measurement of the resin strand thickness on smaller length scales and averaged over a large sample volume. As other techniques that can access protein-scale structural information, such as ISEC, measure the pore size distribution, these two techniques can provide complementary information about the accessible space and the filled space in these resin materials. For HyperCel, the measured radius of gyration of the resin strands is about 34 Å, which corresponds well with mean pore radius measurements via ISEC of about 40 Å<sup>10</sup>. This makes physical sense, as in a random polymer network, one can expect that the pore sizes are of a similar length scale to the characteristic length scale of the polymer network.<sup>43</sup>

For FF, the mean cylinder radius as measured by SANS is 14 Å. This corresponds fairly well to the diameter of the double

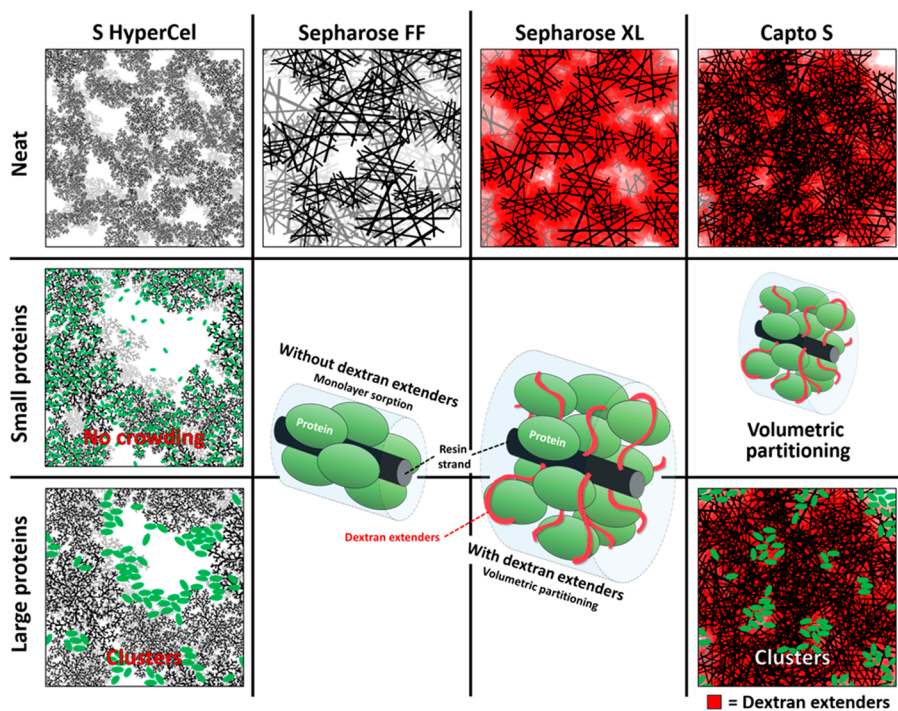


**Figure 4.** Overview of the inferred sorption behavior as a function of resin architecture and protein size. In this work, lysozyme is considered a small protein and lactoferrin and mAbs are considered large proteins.

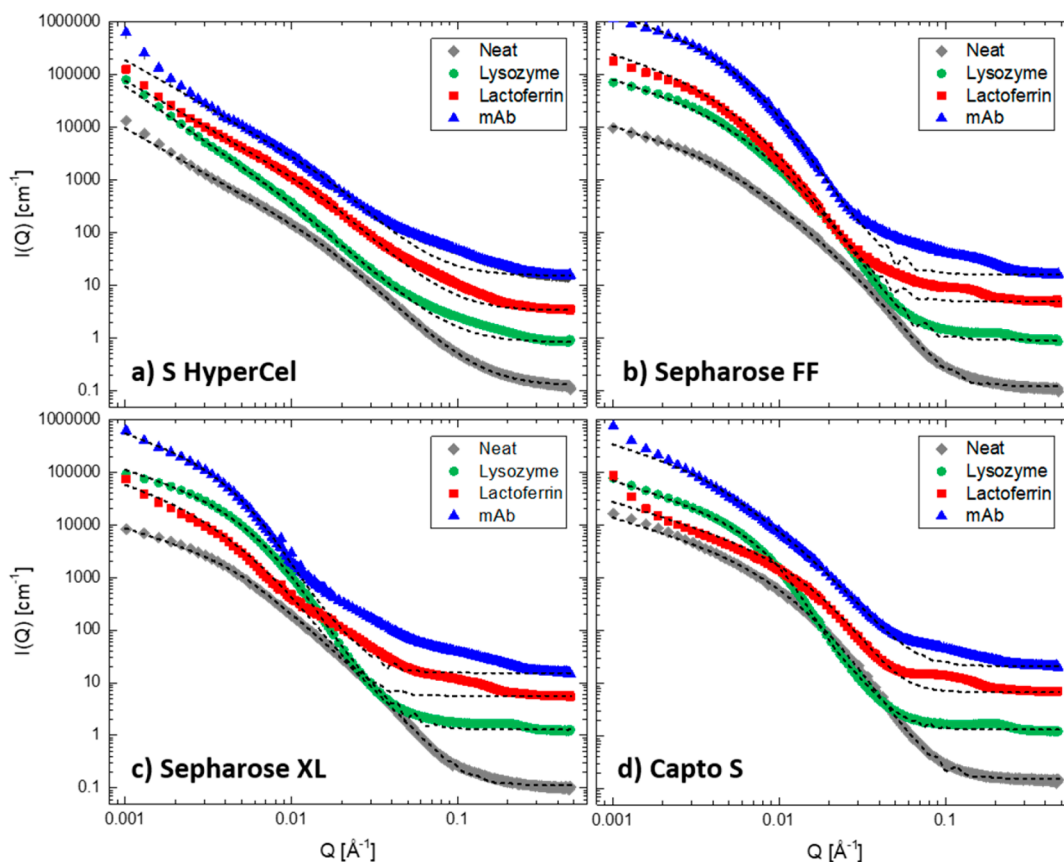


**Figure 5.** Scattering spectra of protein-sorbed chromatographic media at an approximate total ionic strength of 50 mM. Error bars are generally smaller than the symbol size. Successive curves are offset by a factor of 4. Structural model fits are shown by the dashed lines, and were fit only to the background scattering and the low- $Q$  region, up to the  $Q$ -value where the presence of the protein caused an inflection in the scattering spectrum, typically around  $0.03 \text{ \AA}^{-1}$ . Specific fitting ranges are included in the [Supporting Information](#).

helices that compose agarose gels. The fact that SANS can detect these thin strands implies that these helices are sufficiently far apart that they can be observed as distinct scattering objects. Consequently, the observation that these helices form a dense side-by-side assembly within the larger filaments in electron microscopy may be incorrect. Instead, the scattering data suggest that within the filaments, the agarose helices are more loosely distributed. We suspect that these bundle features observed in electron microscopy images probably arise from polymer rearrangement due to resin drying during sample preparation and are not reflective of the media in its native state.

As FF and XL have the same agarose base matrix, the measured difference in cylinder radius between the two materials is due to the dextran modifications in XL. The decrease in the mean cylinder radius from  $14 \text{ \AA}$  in FF to  $3 \text{ \AA}$  in XL and the increase in the polydispersity are consistent with the idea of dextran extending into the pore space, assuming that SANS resolves the individual dextran strands.

In Capto, the significantly larger mean radius of the resin strands of  $51 \text{ \AA}$  is probably caused by the more highly cross-linked base matrix, which makes it similar to HyperCel. Consequently, due to the higher cross-linking, agarose helices in Capto may arrange in the dense side-by-side assembly to form thicker strands as hypothesized before.<sup>38,42</sup> The fact that the dextran extenders are not directly observed in Capto may be due to the fact that larger scattering objects, such as the thicker strands, cause a significantly increased scattering

intensity, which can overwhelm the scattering from the much smaller dextran polymers.

Schematic representations of these interpretations, based on the structural models, are shown in the top panels of [Figure 4](#). In this figure, the long strands in the agarose-based materials represent the helices. Random, single-strand connections between these helices are not explicitly shown, nor are the dextran extenders.

**Scattering Spectra of Protein-Laden Resins.** Lysozyme, lactoferrin, and a mAb were sorbed into the chromatographic resins at different protein loadings by changing the TIS of the solvent among 20, 50, 100, and 200 mM. SANS spectra at 50 mM TIS, at which the protein loading is generally high ([Figure 1](#)), are shown in [Figure 5](#). For each resin, the same models used to fit the neat resins were used to fit the protein-laden resins, and these are shown by the dashed lines in [Figure 5](#). The high- $Q$  region was excluded from the model fits because the contribution from protein monomers was accounted for instead by protein form and structure factors, as discussed in the [Experimental Section](#).

The fitting parameters for the generalized Guinier-Porod model for protein-laden HyperCel at 50 mM are included in [Table 1](#). After protein adsorption, the Porod exponent and radius of gyration, which correspond to the fractal dimension inside and the size of the cellulose strands, do not vary significantly from the values for the neat resin, 2.7 and  $34 \text{ \AA}$ , respectively. For the HyperCel–lysozyme system, the dimension variable, which corresponds to the fractal dimension of the

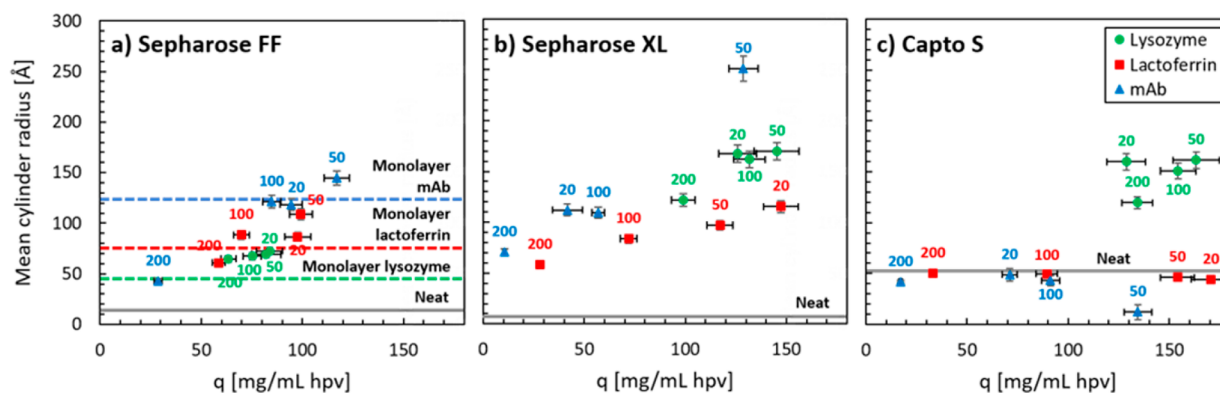


**Figure 6.** Cylinder radii of protein-laden agarose-based resins obtained by fitting SANS data to the polydisperse cylinder model. Labels indicate the approximate total ionic strength of each sample. Gray lines indicate the cylinder radii obtained for the neat media, while colored dashed lines indicate the expected cylinder radius if a uniform layer of protein adsorbs.

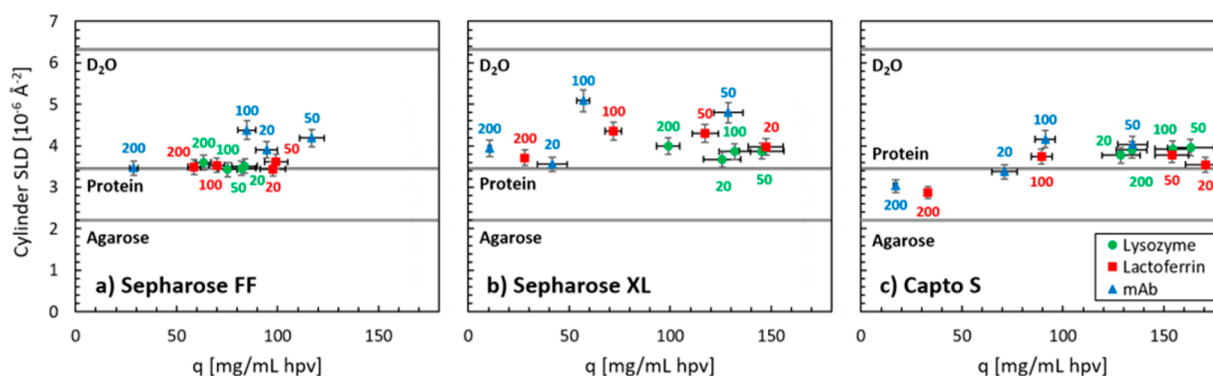


**Figure 7.** Cylinder scattering length densities (SLDs) as obtained from fitting SANS data to the polydisperse cylinder model. Labels indicate the approximate total ionic strength of each sample. Gray lines indicate the SLD of pure  $\text{D}_2\text{O}$  and the approximate SLD of protein and agarose in the sample solvent. Note that the cylinder SLD for the neat media is the value for agarose, as indicated in the figures.

larger-scale resin strand network, increases as a function of the amount of adsorbed protein, going up to 2.4 for the 20 mM lysozyme sample as compared to the 1.8 of the neat resin. However, for the larger proteins the dimension variable does not change after protein adsorption at any TIS value; only the scaling coefficient changes due to variation in the SLDs. Consequently, the HyperCel architecture does not change at all with adsorption of larger proteins, which is illustrated by fixing the Porod exponent and dimension variable for these protein–resin combinations. The only change in the scattering spectrum is the contribution of the protein monomers at high  $Q$  and an upturn at very low  $Q$ , which indicates the presence of larger objects outside the scattering limits.

The fitting parameters for the polydisperse cylinder model for the protein-laden agarose-based resins are the radial polydispersity, the mean cylinder radius and the SLD of the solid cylinder phase. The radial polydispersity is generally around 0.5–0.6 for the protein-laden resins. The mean cylinder radius for each sample and the SLDs of the cylinders as a function of the amount of adsorbed protein are shown in Figures 6 and 7, respectively. The mean cylinder radius generally increases from the value for the neat resins (shown by the gray lines) as more protein is loaded on the resins (Figure 6). This increase in cylinder radius is accompanied by a shift of the SLD from the value for agarose for neat resins to an SLD between the values for pure  $\text{D}_2\text{O}$  and typical proteins (Figure 7).

The high- $Q$  scattering contributions due to protein monomers are compared directly to the expected protein form factors in Figure 8. The symbols in this figure show the experimental scattering spectrum after subtraction of the structural model fit, which corresponds to the difference between the experimental data (symbols) and model fits (dashed lines) in Figure 5. Such subtraction is technically valid only if the two contributions, the structural model and the protein monomer contribution, are strictly uncorrelated, which is not the case here. However, this subtraction is performed here only to highlight the protein contributions in the high- $Q$  region, and deviations due to protein–resin interactions are implicitly included in the effective protein structure factor. In the low- $Q$  region, where the structural model fit describes the experimental scattering well, the subtraction involves two large, almost equal numbers, which typically results in large inherent errors in the data. Consequently, this region of the scattering spectrum can be ignored for  $Q$ -values below those indicated by the black diamonds in Figure 8.

The dashed lines in Figure 8 show the predicted contributions of the presence of proteins solely due to the protein form factors, based on the experimental form factors measured in dilute solution (Figure 2) but scaled to actual protein concentrations within the resins. Significant deviations between the experimental data and the dashed lines indicate the effect of a protein structure factor different from unity, indicating structuring in the distribution of sorbed protein. The dashed vertical lines in Figure 8 indicate the positions of

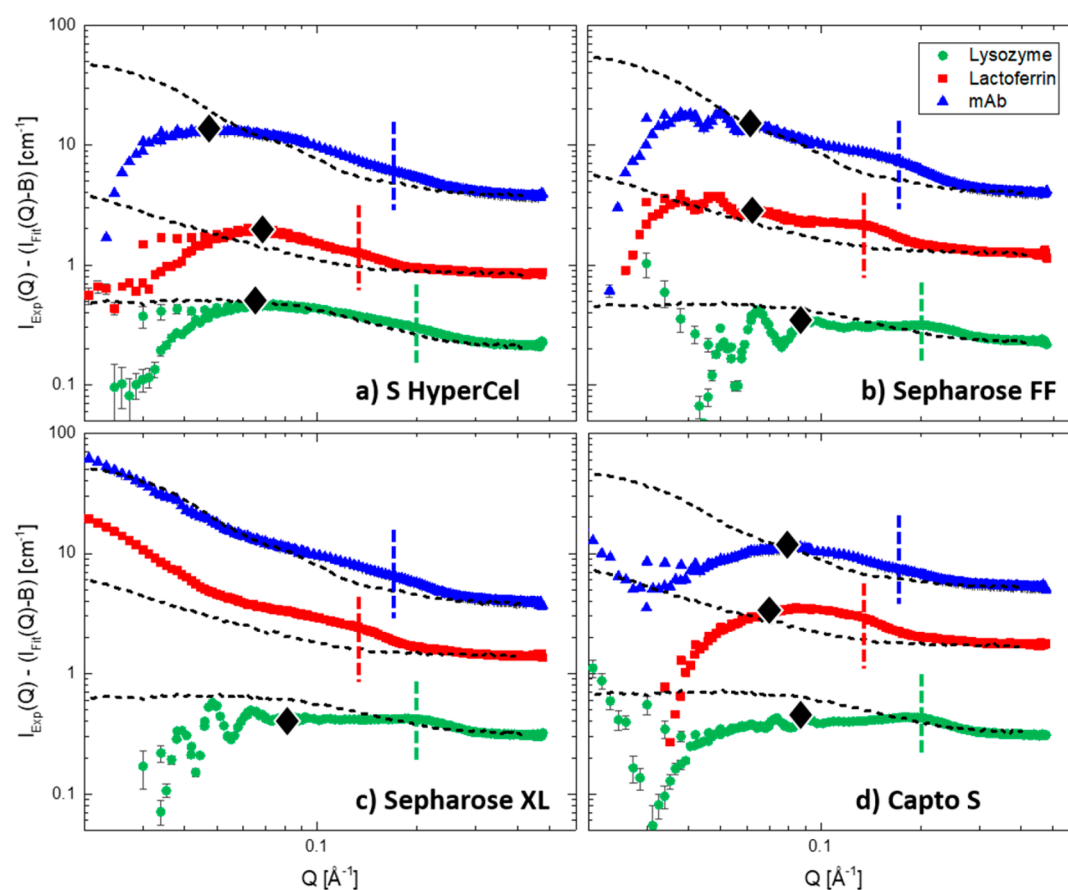


**Figure 8.** Scattering spectra of protein-sorbed chromatographic media after subtraction of the low- $Q$  model fit, at an approximate total ionic strength of 50 mM. Resulting scattering intensity is due to the presence of protein monomers. Predicted scattering intensity due purely to the protein form factor is shown by the dashed lines. Vertical lines show the position of peaks or shoulders in the scattering data, where the difference between the experimental data and the predicted form factor data is generally the highest. These lines are at the same  $Q$ -values in each panel. Black diamonds indicate the  $Q$ -value below which subtraction effects and artifacts become considerable. Error bars due to instrument error are generally smaller than the symbol size. Successive curves are offset by a factor of 4.

peaks or shoulders in the experimental data and are positioned at the same  $Q$ -values in each panel of the figure. These peak positions are summarized in Table 3.

**Table 3. Peak Positions in the Scattering Spectra of the Protein Monomer Contributions**

	lysozyme	lactoferrin	mAb
peak position [ $\text{\AA}^{-1}$ ] <sup>a</sup>	0.20	0.13	0.17
nearest neighbor distance [ $\text{\AA}$ ] <sup>b</sup>	31.4	48.3	37.0
$R_g$ [ $\text{\AA}$ ] <sup>c</sup>	15	30	55

<sup>a</sup>Indicated by the vertical lines in Figure 8 for 50 mM total ionic strength. The same peak positions are observed at different ionic strengths (see the Supporting Information). <sup>b</sup>Calculated from the peak position using eq 4. <sup>c</sup>Calculated using CRYSON.<sup>30</sup>

**Protein Distribution in S HyperCel.** The distribution of lysozyme in HyperCel is found to agree with that observed previously,<sup>17</sup> namely that lysozyme adsorption increases the fractal dimension of the resin network (Table 1), which corresponds to a densification of this fractal network. This indicates that lysozyme is capable of infiltrating into and adsorbing in the smallest pore spaces within the resin. Moreover, the scattering from the lysozyme monomers at high  $Q$ -values corresponds very well to the predicted form factor scattering (Figure 8a). Consequently, contributions from

the structure factor are negligible, which means that there are no significant structural protein–protein or protein–resin interactions. A schematic representation of the inferred distribution of lysozyme in HyperCel, where protein monomers lead to a densification of the fractal network, is shown in the first panel of the second row of Figure 4.

Larger proteins, such as lactoferrin and the mAb, show very different nanoscale distributions in HyperCel. The adsorption of these proteins has no significant effect on either the Porod exponent or the dimensional variable. Hence, larger proteins seem to be excluded from the smallest pore spaces in the fractal resin matrix, but can presumably still attach to the resin at the surface of larger pores. This size-exclusion effect can potentially explain the significantly decreased binding capacity of HyperCel for larger proteins, especially at high TIS. Under these conditions, the cellulose strands that make up the smaller fractal regions within the resin matrix could condense, restricting the available interstitial space for large proteins even more.<sup>16</sup>

Alternatively, our data suggest that large proteins may accumulate locally in specific regions of the pore space, where they partition from the neighboring resin network due to entropic partitioning. Such entropic effects have been demonstrated previously to lead to specific ordering of colloid-polymer systems, including protein systems.<sup>44–46</sup> However, they have not been associated with the partitioning

of proteins in materials such as these chromatographic resins. We argue that instead of solely size-exclusion effects, protein crowding in chromatographic resins may be entropically favored due to depletion or excluded-volume forces.

For these larger proteins, the scattering from the protein monomers at high  $Q$ -values is no longer well-described by the form factor alone (Figure 8a). A significant structure factor is present, indicating the presence of protein–protein or protein–resin interactions indicative of local crowding. Such structuring is observed for all other resin–protein combinations investigated in this paper (Figure 8). Indeed, all high- $Q$  scattering spectra have a significant deviation from the predicted form factor scattering. In particular, all scattering spectra show a scattering peak or shoulder in the same position for a specific protein. The approximate positions are indicated by the vertical lines in Figure 8 and are summarized in Table 3. Note that the vertical line for a given protein is at the same  $Q$ -value in each panel of Figure 8.

Interestingly, these peaks and their positions are similar to those observed in SANS spectra of frozen protein solutions.<sup>47,48</sup> In frozen solutions, proteins are concentrated in dense phases due to the formation of ice crystals. Consequently, the scattering spectra show a protein–protein interaction peak, also termed the nearest-neighbor peak, as the position of the peak is related to the average distance between neighboring protein molecules in the dense phase through eq 4. The average protein–protein distance as obtained from the approximate peak positions in this work are included in Table 3, where they are compared to the radii of gyration of the proteins as obtained from CRYSON.<sup>30</sup> For lysozyme, the interprotein distance corresponds to twice the protein radius, indicating that the protein molecules are in close contact. For lactoferrin, the interprotein distance is slightly smaller than twice the radius of gyration. This is possible as lactoferrin has a two-lobed, dumbbell-like shape (Figure 9) and the protein molecules can stack side by side. This side-by-side configuration is expected to be facilitated by the highly charged patch on one of lactoferrin's lobes, which may allow it to adsorb end-on on the functionalized resin. For mAbs, the interprotein distance is significantly smaller than twice the radius of gyration. Again, this is expected as mAbs are known to interdigitate due to their

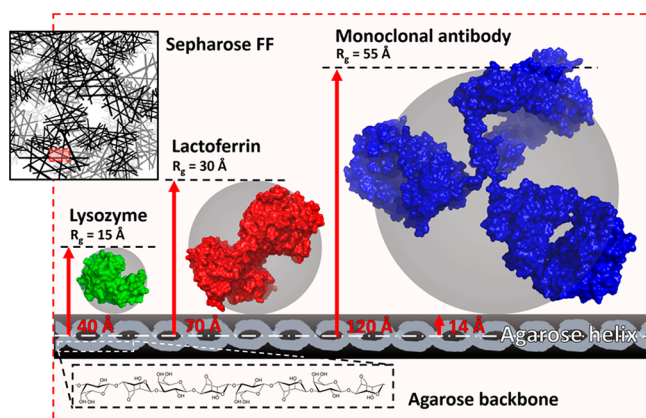


**Figure 9.** Illustration of the effect of protein sorption on the measured radius of an effective cylinder as a function of protein size, assuming that proteins distribute in a monolayer around the resin strands (Figure 4, center left). Protein structures were drawn merely for illustration using PyMOL<sup>49</sup> from the same PDB files used for the CRYSON form factor calculations.

Y-like shape and flexibility, and the interprotein distance is governed by the size of the Fab domains.<sup>48</sup>

These observations support the idea that in HyperCel, lysozyme can infiltrate the fractal resin network, densifying the network but minimizing protein–protein contact. However, larger proteins are excluded from the network and instead form dense phases on the surfaces of the larger pores in the material due to size-exclusion or entropic effects.

**Protein Distribution in Sepharose FF and XL.** Protein adsorption in FF and XL leads to an increase in the cylinder radius obtained from the polydisperse cylinder model. Generally, the cylinder radius increases with increased amounts of adsorbed protein (Figure 6). This increase in the radius is presumably caused by adsorption of the protein on the resin strands. Indeed, the increases in fitted cylinder radii in FF correspond well to the expected values for a monolayer of protein positioned around the strands, as shown by the dashed lines in Figure 6a. These values were estimated from the neat resin radius and the radii of gyration of the proteins as obtained from CRYSON,<sup>30</sup> as shown in Figure 9. In addition, the SLD of the cylinders shifts from the value for agarose for the neat resins to the value for proteins after protein adsorption (Figure 7a). The SLD values for the FF-mAb samples are slightly higher, but this is to be expected as the Y-like shape of the mAbs will lead to significant presence of D<sub>2</sub>O in the cylinder volume.

In comparison, the cylinder radii measured for XL are significantly larger than those for FF (Figure 6b). This indicates that proteins partition in XL throughout the dextran extenders around the base resin strands. The highest values of the observed cylinder radii in XL are about 170 Å for lysozyme and 250 Å for the mAb, which translates to a thickness of the polymer-filled dextran layer of about 160–240 Å, assuming that the base matrix resin strands are equally thick to those in FF. These values correspond well to the thickness of the neat dextran layer as measured by ISEC, which is about 120–190 Å.<sup>7,50</sup> The cylinder SLD values for protein-laden XL are also generally higher than in FF, which is expected as the volumetric partitioning of proteins will lead to increased presence of D<sub>2</sub>O in the cylinder volume. Consequently, proteins form relatively dense phases around the resin strands – as monolayers in the case of FF and by volumetric partitioning in the case of XL, with the dextran included, as is illustrated in the central panels of Figure 4.

This interpretation of the data is further supported by the presence of scattering peaks at high  $Q$  from the sorbed proteins, which are indicative of protein packing (Figure 8 and Table 3). For FF in particular, the peaks are fairly well-defined, indicating that the range of interprotein distances is fairly narrow. For XL, the peaks are slightly broader, indicating that the proteins are more heterogeneously distributed. Such behavior is expected as interprotein distances will be more strictly defined in monolayer adsorption as compared to volumetric partitioning, not least because of the presence of the dextran.

Electron microscopy typically shows clusters or lumps of protein on larger length scales than those observed here.<sup>9,11</sup> Again, this may be due to insufficient resolution of the technique and/or to significant structural changes of the resin during sample processing. SANS measurements show that protein molecules distribute within the resins on characteristic length scales on the order of nanometers, which is smaller than what has been observed in electron microscopy.

**Protein Distribution in Capto S.** Protein adsorption in Capto shows similarities to that in both XL and HyperCel.

Lysozyme adsorption in Capto S shows the same behavior as that in XL, with similar cylinder radii, SLDs, and interaction peaks. Consequently, the interpretation is the same as for that resin. However, lactoferrin and mAb adsorption in Capto is characterized by almost no change in the measured cylinder radius (Figure 6c). Similarly to the case for HyperCel, these larger proteins seem to be excluded from at least the smallest pores in the resin matrix or within the dextran layer, making them unable to bind close to the base resin strands. However, they can presumably still attach to dextran extenders at the surface of larger pores, as is shown in the bottom right panel of Figure 4. Alternatively, similar to the behavior in HyperCel, these larger proteins in Capto may crowd due to entropic partitioning. Such partitioning would help to explain the differences in protein transport observed between traditional and dextran-modified resins. For dextran-modified resins, it has been proposed that protein uptake occurs with a sharp uptake front with incomplete saturation.<sup>8</sup> The reason for the incomplete saturation was hypothesized to be the inefficient packing of the protein, which can rearrange over time to accommodate more protein. Entropic partitioning is a possible mechanistic explanation for this protein rearrangement.

## CONCLUSIONS

Small-angle neutron scattering allows in situ characterization of resin architectures and the internal protein distributions, with protein-scale resolution. The results obtained here show that protein molecules arrange in chromatographic resins on nanometer length scales, smaller than what has previously been observed with conventional characterization techniques, and the results reflect the variability of these arrangements that would be expected as a function of resin architecture and protein size. Dextran-modification or the fractal architectures of cellulose-based materials can increase protein loading due to the possibility of volumetric partitioning. However, highly cross-linked chromatographic materials can exhibit crowding behavior of larger proteins such as lactoferrin and mAbs due to size-exclusion or entropic partitioning effects. While these observations confirm the structural origins of the increased binding capacities in the resins investigated, they could also explain the higher salt sensitivity of larger proteins in these materials and their distinct transport behavior. Consequently, these observations can be used to guide design of chromatographic resins. Moreover, the techniques presented here allow characterization of novel and future resin materials, and the mechanisms inferred to contribute to the observed behavior can certainly be applicable in other systems.

## ASSOCIATED CONTENT

### Supporting Information

The Supporting Information is available free of charge on the ACS Publications website at DOI: [10.1021/acs.langmuir.7b03289](https://doi.org/10.1021/acs.langmuir.7b03289).

Scattering spectra and fitting parameters for all resin–protein combinations and loading conditions (PDF)

## AUTHOR INFORMATION

### Corresponding Author

\*E-mail: [lenhoff@udel.edu](mailto:lenhoff@udel.edu). Telephone: 302-831-8989.

### ORCID

Norman J. Wagner: 0000-0001-9565-619X

Abraham M. Lenhoff: 0000-0002-7831-219X

## Notes

The authors declare no competing financial interest.

## ACKNOWLEDGMENTS

The authors thank Amgen for donating the monoclonal antibody. This work was supported by National Science Foundation Grant No. CBET-1263966. N.J.W. acknowledges support under cooperative agreements # 70NANB12H239 and 70NANB15H260 from NIST, U.S. Department of Commerce. The authors acknowledge the support of the National Institute of Standards and Technology, U.S. Department of Commerce, in providing the neutron research facilities used in this work. This work utilized facilities supported in part by the National Science Foundation under Agreement No. DMR-0944772. The statements, findings, conclusions and recommendations are those of the authors and do not necessarily reflect the view of NIST or the U.S. Department of Commerce.

## REFERENCES

- (1) Thömmes, J. Investigations on Protein Adsorption to Agarose-Dextran Composite Media. *Biotechnol. Bioeng.* **1999**, *62* (3), 358–362.
- (2) Cooper, C. L.; Dubin, P. L.; Kayitmazer, A. B.; Turksen, S. Polyelectrolyte–protein Complexes. *Curr. Opin. Colloid Interface Sci.* **2005**, *10* (1–2), 52–78.
- (3) Johansson, H.-O.; Van Alstine, J. M. Modeling of Protein Interactions with Surface-Grafted Charged Polymers. Correlations between Statistical Molecular Modeling and a Mean Field Approach. *Langmuir* **2006**, *22* (21), 8920–8930.
- (4) Lenhoff, A. M. Protein Adsorption and Transport in Polymer-Functionalized Ion-Exchangers. *J. Chromatogr. A* **2011**, *1218* (49), 8748–8759.
- (5) Müller, E. Properties and Characterization of High Capacity Resins for Biochromatography. *Chem. Eng. Technol.* **2005**, *28* (11), 1295–1305.
- (6) Yao, Y.; Lenhoff, A. M. Pore Size Distributions of Ion Exchangers and Relation to Protein Binding Capacity. *J. Chromatogr. A* **2006**, *1126* (1–2), 107–119.
- (7) Bowes, B. D.; Koku, H.; Czymmek, K. J.; Lenhoff, A. M. Protein Adsorption and Transport in Dextran-Modified Ion-Exchange Media. I: Adsorption. *J. Chromatogr. A* **2009**, *1216* (45), 7774–7784.
- (8) Bowes, B. D.; Lenhoff, A. M. Protein Adsorption and Transport in Dextran-Modified Ion-Exchange Media. III. Effects of Resin Charge Density and Dextran Content on Adsorption and Intraparticle Uptake. *J. Chromatogr. A* **2011**, *1218* (40), 7180–7188.
- (9) Koku, H. Microstructure-Based Analysis and Simulation of Flow and Mass Transfer in Chromatographic Stationary Phases. Ph.D. Dissertation, University of Delaware, 2011.
- (10) Angelo, J. M.; Cvetkovic, A.; Gantier, R.; Lenhoff, A. M. Characterization of Cross-Linked Cellulosic Ion-Exchange Adsorbents: 1. Structural Properties. *J. Chromatogr. A* **2013**, *1319*, 46–56.
- (11) Angelo, J. M.; Cvetkovic, A.; Gantier, R.; Lenhoff, A. M. Characterization of Cross-Linked Cellulosic Ion-Exchange Adsorbents: 2. Protein Sorption and Transport. *J. Chromatogr. A* **2016**, *1438*, 100–112.
- (12) Hahn, R. Methods for Characterization of Biochromatography Media. *J. Sep. Sci.* **2012**, *35* (22), 3001–3032.
- (13) Yao, Y.; Lenhoff, A. M. Determination of Pore Size Distributions of Porous Chromatographic Adsorbents by Inverse Size-Exclusion Chromatography. *J. Chromatogr. A* **2004**, *1037* (1–2), 273–282.
- (14) Tao, Y.; Carta, G.; Ferreira, G.; Robbins, D. Adsorption of Deamidated Antibody Variants on Macroporous and Dextran-Grafted Cation Exchangers: I. Adsorption Equilibrium. *J. Chromatogr. A* **2011**, *1218* (11), 1519–1529.
- (15) Ubiera, A. R.; Carta, G. Radiotracer Measurements of Protein Mass Transfer: Kinetics in Ion Exchange Media. *Biotechnol. J.* **2006**, *1* (6), 665–674.

- (16) DePhillips, P.; Lenhoff, A. M. Pore Size Distributions of Cation-Exchange Adsorbents Determined by Inverse Size-Exclusion Chromatography. *J. Chromatogr. A* **2000**, *883* (1–2), 39–54.
- (17) Koshari, S. H. S.; Wagner, N. J.; Lenhoff, A. M. Characterization of Lysozyme Adsorption in Cellulosic Chromatographic Materials Using Small-Angle Neutron Scattering. *J. Chromatogr. A* **2015**, *1399*, 45–52.
- (18) Krueger, S.; Andrews, A. P.; Nossal, R. Small Angle Neutron Scattering Studies of Structural Characteristics of Agarose Gels. *Biophys. Chem.* **1994**, *53* (1–2), 85–94.
- (19) Svergun, D. I.; Koch, M. H. J. Small-Angle Scattering Studies of Biological Macromolecules in Solution. *Rep. Prog. Phys.* **2003**, *66* (10), 1735–1782.
- (20) Grillo, I. Small-Angle Neutron Scattering and Applications in Soft Condensed Matter. In *Soft-Matter Characterization*; Borsali, R., Pecora, R., Eds.; Springer: Berlin, 2008; pp 705–764.
- (21) Hammouda, B. *Probing Nanoscale Structures - The SANS Toolbox*; National Institute of Standards and Technology: Gaithersburg, MD, 2010.
- (22) Sivia, D. S. *Elementary Scattering Theory*, First ed.; Oxford University Press: New York, 2011.
- (23) Koshari, S. H. S. Characterization of Lysozyme Adsorption in Cellulosic Chromatographic Materials Using Small-Angle Neutron Scattering. Master's Thesis, University of Delaware, 2014.
- (24) Bowes, B. D.; Traylor, S. J.; Timmick, S. M.; Czymmek, K. J.; Lenhoff, A. M. Insights into Protein Sorption and Desorption on Dextran-Modified Ion-Exchange Media. *Chem. Eng. Technol.* **2012**, *35* (1), 91–101.
- (25) Harinarayan, C.; Mueller, J.; Ljunglöf, A.; Fahrner, R.; Van Alstine, J.; van Reis, R. An Exclusion Mechanism in Ion Exchange Chromatography. *Biotechnol. Bioeng.* **2006**, *95* (5), 775–787.
- (26) Glinka, C. J.; Barker, J. G.; Hammouda, B.; Krueger, S.; Moyer, J. J.; Orts, W. J. The 30 M Small-Angle Neutron Scattering Instruments at the National Institute of Standards and Technology. *J. Appl. Crystallogr.* **1998**, *31* (3), 430–445.
- (27) Kline, S. R. Reduction and Analysis of SANS and USANS Data Using IGOR Pro. *J. Appl. Crystallogr.* **2006**, *39* (6), 895–900.
- (28) Hammouda, B. A New Guinier–Porod Model. *J. Appl. Crystallogr.* **2010**, *43* (4), 716–719.
- (29) Guinier, A.; Fournet, G. *Small-Angle Scattering of X-Rays*, first ed.; John Wiley and Sons: New York, 1955.
- (30) Svergun, D. I.; Richard, S.; Koch, M. H. J.; Sayers, Z.; Kuprin, S.; Zaccai, G. Protein Hydration in Solution: Experimental Observation by X-Ray and Neutron Scattering. *Proc. Natl. Acad. Sci. U. S. A.* **1998**, *95* (5), 2267–2272.
- (31) Berman, H. M.; Westbrook, J.; Feng, Z.; Gilliland, G.; Bhat, T. N.; Weissig, H.; Shindyalov, I. N.; Bourne, P. E. *The Protein Data Bank*; [www.rcsb.org](http://www.rcsb.org).
- (32) Diamond, R. Real-Space Refinement of the Structure of Hen Egg-White Lysozyme. *J. Mol. Biol.* **1974**, *82* (3), 371–391.
- (33) Thomassen, E. A. J.; van Veen, H. A.; van Berkel, P. H. C.; Nuijens, J. H.; Abrahams, J. P. The Protein Structure of Recombinant Human Lactoferrin Produced in the Milk of Transgenic Cows Closely Matches the Structure of Human Milk-Derived Lactoferrin. *Transgenic Res.* **2005**, *14* (4), 397–405.
- (34) Harris, L. J.; Larson, S. B.; Hasel, K. W.; McPherson, A. Refined Structure of an Intact IgG2a Monoclonal Antibody. *Biochemistry* **1997**, *36* (7), 1581–1597.
- (35) Sears, V. F. Neutron Scattering Lengths and Cross Sections. *Neutron News* **1992**, *3* (3), 26–37.
- (36) Kienzle, P. *Neutron activation and scattering calculator*; <http://www.ncnr.nist.gov/resources/activation/>.
- (37) Svergun, D.; Barberato, C.; Koch, M. CRY SOL - a Program to Evaluate X-Ray Solution Scattering of Biological Macromolecules from Atomic Coordinates. *J. Appl. Crystallogr.* **1995**, *28*, 768–773.
- (38) Arnott, S.; Fulmer, A.; Scott, W. E.; Dea, I. C. M.; Moorhouse, R.; Rees, D. A. The Agarose Double Helix and Its Function in Agarose Gel Structure. *J. Mol. Biol.* **1974**, *90* (2), 269–284.
- (39) Foord, S. A.; Atkins, E. D. Y. New X-Ray Diffraction Results from Agarose: Extended Single Helix Structures and Implications for Gelation Mechanism. *Biopolymers* **1989**, *28* (8), 1345–1365.
- (40) Schafer, S. E.; Stevens, E. S. A Reexamination of the Double-Helix Model for Agarose Gels Using Optical Rotation. *Biopolymers* **1995**, *36*, 103–108.
- (41) Guenet, J.-M.; Rochas, C. Agarose Sols and Gels Revisited. *Macromol. Symp.* **2006**, *242* (1), 65–70.
- (42) Amsterdam, A.; Er-El, Z.; Shaltiel, S. Ultrastructure of Beaded Agarose. *Arch. Biochem. Biophys.* **1975**, *171* (2), 673–677.
- (43) Ogston, A. G. The Spaces in a Uniform Random Suspension of Fibres. *Trans. Faraday Soc.* **1958**, *54*, 1754.
- (44) Adams, M.; Dogic, Z.; Keller, S. L.; Fraden, S. Entropically Driven Microphase Transitions in Mixtures of Colloidal Rods and Spheres. *Nature* **1998**, *393* (6683), 349–352.
- (45) Dogic, Z.; Fraden, S. Ordered Phases of Filamentous Viruses. *Curr. Opin. Colloid Interface Sci.* **2006**, *11* (1), 47–55.
- (46) Zhou, H.-X.; Rivas, G.; Minton, A. P. Macromolecular Crowding and Confinement: Biochemical, Biophysical, and Potential Physiological Consequences. *Annu. Rev. Biophys.* **2008**, *37* (1), 375–397.
- (47) Curtis, J. E.; Nanda, H.; Khodadadi, S.; Cicerone, M.; Lee, H. J.; McAuley, A.; Krueger, S. Small-Angle Neutron Scattering Study of Protein Crowding in Liquid and Solid Phases: Lysozyme in Aqueous Solution, Frozen Solution, and Carbohydrate Powders. *J. Phys. Chem. B* **2012**, *116* (32), 9653–9667.
- (48) Castellanos, M. M.; Clark, N. J.; Watson, M. C.; Krueger, S.; McAuley, A.; Curtis, J. E. Role of Molecular Flexibility and Colloidal Descriptions of Proteins in Crowded Environments from Small-Angle Scattering. *J. Phys. Chem. B* **2016**, *120* (49), 12511–12518.
- (49) DeLano, W. L. *The PyMOL Molecular Graphics System*; DeLano Scientific: San Carlos, CA, 2002.
- (50) Angelo, J. M. Mechanisms Underlying Protein Sorption and Transport within Polysaccharide-Based Stationary Phases for Ion-Exchange Chromatography. Ph.D. Dissertation, University of Delaware, 2016.

#### ■ NOTE ADDED AFTER ASAP PUBLICATION

This paper was published ASAP on December 29, 2017, with an incorrect value in the Methods section and with other minor errors in the text. The corrected version was reposted on January 4, 2018.